Bioactive Materials 6 (2021) 1242–1254

Contents lists available at ScienceDirect

Bioactive Materials

journal homepage: www.sciencedirect.com/journal/bioactive-materials

Bone tissue regeneration: The role of finely tuned pore architecture of bioactive scaffolds before clinical translation

Ronghuan Wu [a,1], Yifan Li [a,1], Miaoda Shen [a], Xianyan Yang [b], Lei Zhang [c], Xiurong Ke [c], Guojing Yang [c], Changyou Gao [b], Zhongru Gou [b,*], Sanzhong Xu [a,**]

[a] Department of Orthopedics, The First Affiliated Hospital, Zhejiang University School of Medicine, Hangzhou, 310003, China
[b] Bio-nanomaterials and Regenerative Medicine Research Division, Zhejiang-California International Nanosystem Institute, Zhejiang University, Hangzhou, 310058, China
[c] Rui'an People's Hospital & the 3rd Hospital Affiliated to Wenzhou Medical University, Rui' An, 325200, China

ARTICLE INFO

Keywords:
Pore structural parameter
Bone regeneration efficiency
Precise manufacturing
Porous scaffolds
Tissue engineering

ABSTRACT

Spatial dimension of pores and interconnection in macroporous scaffolds is of particular importance in facilitating endogenous cell migration and bone tissue ingrowth. However, it is still a challenge to widely tune structure parameters of scaffolds by conventional methods because of inevitable pore geometrical deformation and poor pore interconnectivity. Here, the long-term *in vivo* biological performances of nonstoichiometric bioceramic scaffolds with different pore dimensions were assessed in critical-size femoral bone defect model. The 6% Mg-substituted wollastonite (CSi-Mg6) powders were prepared via wet-chemical precipitation and the scaffolds elaborately printed by ceramic stereolithography, displaying designed constant pore strut and tailorable pore height (200, 320, 450, 600 μm), were investigated thoroughly in the bone regeneration process. Together with detailed structural stability and mechanical properties were collaboratively outlined. Both μCT and histological analyses indicated that bone tissue ingrowth was retarded in 200 μm scaffolds in the whole stage (2–16 weeks) but the 320 μm scaffolds showed appreciable bone tissue in the center of porous constructs at 6–10 weeks and matured bone tissue were uniformly invaded in the whole pore networks at 16 weeks. Interestingly, the neotissue ingrowth was facilitated in the 450 μm and 600 μm scaffolds after 2 weeks and higher extent of bone regeneration and remodeling at the later stage. These new findings provide critical information on how engineered porous architecture impact bone regeneration *in vivo*. Simultaneously, this study shows important implications for optimizing the porous scaffolds design by advanced additive manufacture technique to match the clinical translation with high performance.

1. Introduction

The scaffold is the centerpiece of bone tissue engineering efforts, and its design and properties are of paramount importance [1]. First and foremost, the chemical composition and the role of three-dimensional (3D) pore architectures of scaffolds is of particular importance in treating load-bearing bone defects when the damage is too large that its self-healing response is unable to bridge the defect without the aid of macroporous substrates. Second, porosity of scaffolds should be close to trabecular bones (ranging from 50% to 90%) and allows adequate diffusion of nutrients to cells. Last but not the least, it is well acknowledged that pore size influences tissue regeneration while pore interconnection dramatically affects nutrient transport and biodegradation kinetics [2]. Accordingly, constructing macroporous scaffolds that benefit bone tissue ingrowth is an ongoing pursuit in bone repair areas [3–6].

Conventionally, biomaterial implants include not only the porous scaffolds but also the growth factors, functional drugs, or osteogenic cells that could stimulate and even accelerate the bone repair process [7]. With the wide investigation concerning the effects of geometrical

* Corresponding author. Zhejiang-California International Nanosystems Institute Zhejiang University, Hangzhou, Zhejiang Province, 310058, China
** Corresponding author. Department of Orthopedics, the First Affiliated Hospital Zhejiang University School of Medicine 79# Qingchun Road, Hangzhou, Zhejiang Province, 310003, China
E-mail addresses: zhrgou@zju.edu.cn (Z. Gou), xusanzhong@zju.edu.cn (S. Xu).
[1] These authors contributed equally.

https://doi.org/10.1016/j.bioactmat.2020.11.003
Received 21 September 2020; Received in revised form 31 October 2020; Accepted 1 November 2020
Available online 7 November 2020

features of scaffold materials, it is agreed that accelerating bone repair is not limited to the biologically derived molecules [8–10]. The scaffold itself should be optimally designed not only to 'conduct' the unhindered vascularization and tissue ingrowth, but also to 'enhance' these processes [11]. Hence, the scaffolds should be made of strength-strong bioactive material and endowed with macropore structures for nutrition migration, tissue cell adhesion and new bone tissue growth and turnover [12,13].

Till now, some investigations show that a critical pore size and interconnectivity may determine the angiogenesis and ultimately facilitate bone tissue growth [14–17]. For instance, Choi et al. found the inverse opal scaffolds with small pores (<200 μm) facilitate high-density small vessel formation with poor penetration depth; by contrast, the scaffolds with large pores (>200 μm) are advantageous for the formation of low-density large blood vessels with deep penetration depth. In addition, it has been revealed that one hundred microns is the minimum pore size which is beneficial for successful progression of bone regeneration [14]. A scaffold with smaller pore size and/or less interconnected structure may be unable to provide enough space for bone ingrowth or be incapable of providing enough space for material transport across the scaffold. As have been extensively studied elsewhere, there are some contradictory results involving bone regeneration efficiency in the scaffolds with different pore architectures, including pore size, interconnectivity and porosity [16,18]. Most of studies are performed in the early stages *in vivo*, but there is limited evidence from such investigations that can confirm the importance of pore dimension in the whole bone repair stage. Although a variety of porous scaffold fabrication techniques have been developed, for instance, addition of porogen [19], foam replicating [20], freeze-casting and so on [21], were widely studied. Unfortunately, these techniques showed some shortcomings due to the difficulties in customizing external complex shape of scaffolds and internal regular pore shape, size, as well as poor connectivity [3,9,22].

Recently, computer-aided design (CAD) and additive manufacture (AM) technology have remarkably enhanced the capability to produce macroporous scaffolds with controllable pore geometries, which has resulted in more interest in developing innovative pore architecture fabrication [23,24]. It is confirmed that 3D printing technology shows better ability to accurately control the (gradient) pore size and porosity of (multilayer) scaffolds [25–27]. The porous structure of tissue-engineering scaffolds with precisely tailored pore sizes can be realized using ceramic stereolithography [28–30]. Therefore, this triguing technique is favorable for fabricating certain pore features and studying different classes of pore dimensions that could potentially affect bone regeneration.

In order to understand the effect of pore dimension on bone tissue growth efficiency, the porous structures of bioactive scaffolds have to be maintained stably resistant to fast biodegradation. Sintered Mg-doped calcium silicate (CSi-Mg) porous scaffolds [31] have recently become confirmed available and biodegradable slowly. In our previous study using robocast CSi-Mg scaffolds [32], bone tissue regeneration in macroporous scaffolds could hardly proceed concentrically to the center pores due to the limited opening pores in the side-wall of scaffolds. However, their pore structures can be easily changed in the process of stereolithography manufacture.

To clarify the above concerns, it is reasonable to postulate that a long-term implantation study *in vivo* may be helpful for capturing the whole bone repair stages and correctly conclude the pore architectures do influence the progress of bone tissue growth. Based on this hypothesis, the porous scaffolds with cubic pores were analyzed both from their pore architectures based on 3D μCT reconstruction and from critical-sized bone defect model studies. On the basis of the data obtained, we proposed two new indices for the design of pore parameters of 3D printing bioceramic scaffolds and assessment of bone tissue growth in the entire scaffolds.

2. Materials and methods

2.1. Synthesis of the bioceramic powders

The inorganic salts (analytic reagent) were bought from Sinopharm Reagent Co., Shanghai, and used directly without any pre-treatment. The resin (containing curable monomers or oligomers, photo-initiators and dispersant) was provided by Ten Dimensions Technology Co., China. The 6% Mg-substituted wollastonite (CSi-Mg6) bioceramic powders were prepared through a wet-chemical co-precipitation as reported previously [33]. The superfine powders (<5 μm in particle size) were obtained by high-energy ball milling the calcined powders for 6 h. The phase composition was confirmed by X-ray diffraction (XRD, Rigaku, Japan) analysis.

2.2. Fabrication of CSi-Mg6 scaffolds by ceramic stereolithography

The suspensions were prepared by mixing 60% CSi-Mg6 powders and 40% resin and followed by ball milling for 30 min [34]. For 3D stereolithography of the bioceramic scaffolds, the wavelength of the stereolithography apparatus (Ten Dimensions Technology Co., China) used for the curing ultraviolet (UV) light was 405 nm. The cured layer was placed on the glass sheet and the UV light was sourced from below the layer (see Fig. 1A). The cured layers, with a thickness of 200 μm, were manufactured. Four groups of cubic-pore scaffold model (Ø 6.5 × 8.0 mm) with 3D periodic porous architectures (500 × 500 × H mm) of different pore height (H) from 200 to 600 μm (see Fig. 1B) was designed using the CAD software. Different plotting parameters of the printed scaffolds including theoretical porosity and pore size were calculated (see Table 1). The printed samples were washed ultrasonically in deionized water and followed by drying at 60 °C. Finally, the porous bodies were sintered in a muffle furnace at a target temperature of 1150 °C for 3 h (the heating rate is 2 °C/min while maintaining at 480 °C for 60 min). The sintered bioceramic scaffolds with *different pore heights* were denoted as H200, H320, H450, and H600, respectively.

2.3. Morphology, structure and mechanical analysis

The linear shrinkage before and after sintering was determined by measuring the diameter and height of bioceramic scaffolds. The external morphology of scaffolds was observed by optical microscopy (Olympus). The surface and fracture microstructures of scaffolds were investigated by scanning electron microscopy (SEM, S-4800, Hitachi; Japan). The compressive strength of bioceramic scaffolds (n = 6) was measured along the vertical Z direction by a universal testing machine (Instron 5566). The crosshead speed was set to 0.5 mm/min according to the procedure described in ASTM C773-88. The compressive modulus was determined from the linear region of the stress–strain curves.

2.4. Porosity analysis

The volume and pore strut of porous architecture was taken from CAD software and used to determine the theoretical porosity of the modeled scaffold samples. Then, one zero-damage method was used to measure the real porosities of the bioceramic scaffolds. Briefly speaking, the mass (m_1) of sintered scaffolds was weighed, respectively, and then the diameter (D) and height (H) were also measured by using Vernier caliper. The real porosity of the scaffolds (n = 6) could be calculated using the equation [35]: $Porosity = (1- m_s/(\pi\rho_0 (D/2)^2 H)) \times 100\%$, where m_s, and ρ_0 were the mass of the sample and density of wollastonite (2.96 g/mm^3).

2.5. 2D/3d microstructure analysis

The 2D/3D pore architectures of the sintered scaffolds (n = 3) was reconstructed by Micro-computed tomography (vivaCT 100, Scanco

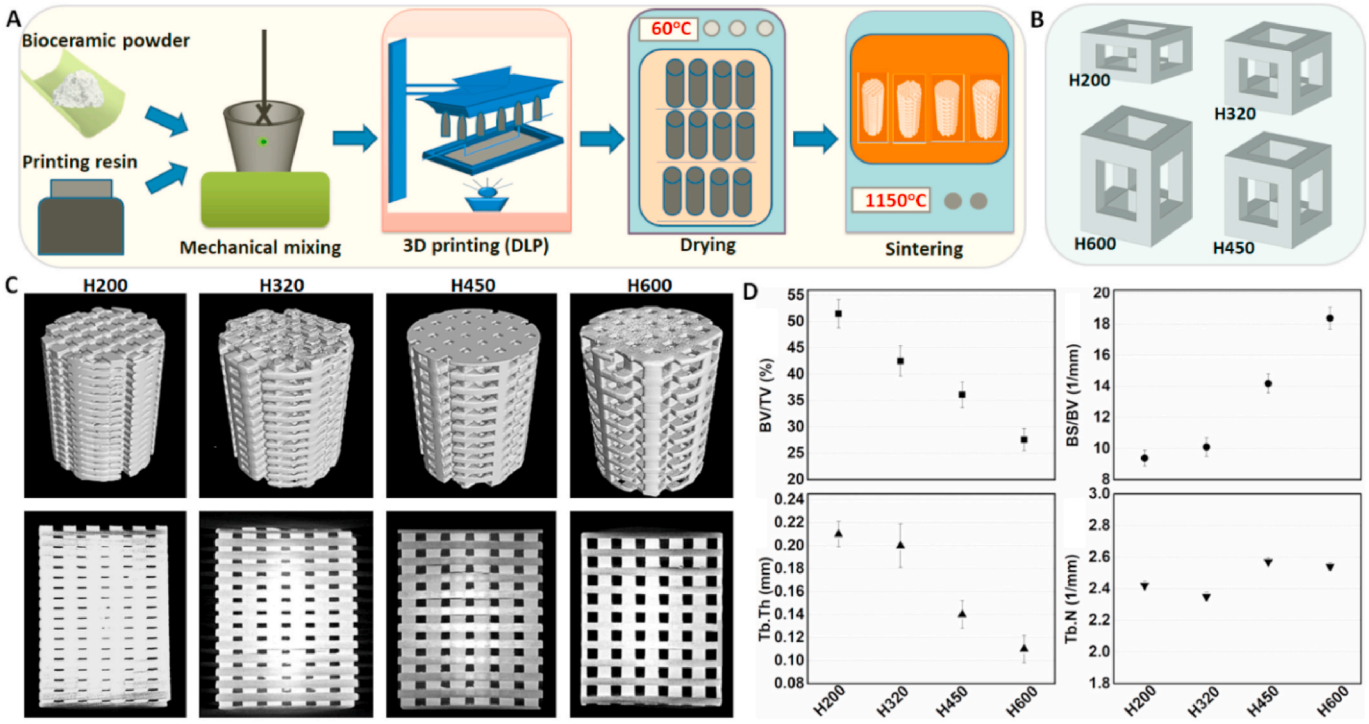

Fig. 1. (A) Schematic preparation process of bioceramic scaffolds by stereolithography technique, (B) CAD-designing four types of repeating unit cells with different cell height (~200, 320, 450, and 600 μm in height), (C) 2D/3D visualization obtained μCT-scanning of sintered scaffolds with tuned pore architectures, and (D) quantitative data of the pore structure parameters by μCT analysis.

Table 1
Physicochemical properties of the bioceramic scaffolds (Ø 6.5 mm × 8.5 mm in CAD model).

Materials	CAD-mode pore parameters				Real pore parameters			
	X–Y pore size (μm)	Z pore size (μm)	Porosity (%)	Specific surface area (m^{-1})	X–Y pore size (μm)	Z pore size (μm)	Porosity (%)	Specific surface area (m^{-1})
H200	500 × 500	550 × 200	48.20	7.62	440 ± 8 × 440 ± 12	480 ± 14 × 130 ± 12	46.2 ± 1.0	6.39 ± 0.78
H320	500 × 500	550 × 320	52.82	8.14	430 ± 6 × 430 ± 10	470 ± 16 × 250 ± 16	48.9 ± 1.4	7.28 ± 0.62
H450	500 × 500	550 × 450	55.92	8.95	430 ± 8 × 430 ± 14	470 ± 18 × 380 ± 21	51.8 ± 1.7	7.68 ± 0.43
H600	500 × 500	550 × 600	59.46	8.20	420 ± 5 × 420 ± 16	470 ± 14 × 540 ± 18	54.0 ± 2.2	7.45 ± 0.66

Medical, Switzerland) at 14 μm resolution and exposure time of 3000 ms. The images were reconstructed by supporting software (Volume Graphics MAX, Volume Graphics, Germany) to generate 2D/3D images (Ø ~6.0 × 7.2 mm) for morphometric analysis of pore architectures of scaffolds. The quantitative data of pore parameters including strut volume-to-total volume (BV/TV), strut thickness (Tb·Th), strut number (Tb·N), and strut surface-to-strut volume (BS/BV) were calculated by the Volume Graphics MAX 3.0.2 software. The specific surface area of the sintered scaffolds was also estimated using quantitative 3D evaluation program included with the MicView software package after μCT reconstruction.

2.6. Bio-dissolution analysis in vitro

The cylindrical scaffolds (m_0; $n = 6$) were weighed and immersed in Tris buffer (pH 7.4) with a solid-to-liquid ratio of 1.0 g/50 ml at 37 °C. After immersing every two weeks from 2 to 8 weeks, the buffer (1.0 ml) was extracted for examination the ionic release concentrations (Si, Ca,

Mg) by inductively coupled plasma measurement (ICP; Thermo, USA), and equivalent fresh buffer was added into the immersion medium. At 4 and 8 weeks, the scaffold samples were washed with absolute ethanol and then dried at 80 °C for 12 h before weighing (m_t). The mass decrease was expressed as: mass loss = $m_t/m_0 \times 100\%$.

2.7. Bone regeneration and repair evaluation in vivo

2.7.1. Scaffold implantation and specimen harvesting

All animal operations and experiments were approved by the Experimental Animals Ethics Committee of Zhejiang University (No.866). The male New Zealand white rabbits (~3.2 kg; $n = 60$) were divided into four groups randomly. All of the rabbits were placed in steel cages singly about one week for adaptation before surgery. After general intravenous anesthesia by injection of 3% sodium phenobarbital (Merck, Germany) at 1.0 mg/kg, the implanting surgery was performed to bilateral distal femurs of all the rabbits under rigorous aseptic conditions. A 3-cm longitudinal skin incision was made on the lateral femoral condyle of each leg. Then, a critical size defect (Ø ~6.0 × 7.2 mm) was structured on the bilateral femoral condyles by a dental drill. All defects were made oriented vertical to the longitudinal and sagittal axes of the femur. Afterwards, the scaffolds were filled into the defects, and the surgery site was rinsed with normal saline and the incision was sutured layer by layer. The rabbits were allowed to move freely in the cage after the operation and received an intramuscular injection of penicillin for 3 days. The femoral bone specimens were collected at 2, 4, 6, 10, and 16 weeks after rabbits were sacrificed by deep anesthesia.

2.7.2. Radiological examination by X-ray

The radiological examination on new bone formation and material biodegradation was performed by an X-ray imaging system (XPERT; KUBTEC, USA) under 50 KV and 100 μA. The general X-ray films were taken both frontally and laterally by the X-ray system. Then, the films were transported to the computer for the further analysis through the imaging software of Image-pro Plus (IPP 6.0, Media Cybernetics, USA). The quantitative analysis of the residual material volume versus total initially defect volume was expressed as RV/TV ($n = 5$).

2.7.3. μCT scanning analysis

To assess the bone regeneration efficiency, the μCT (micro-computed tomography) scanning was applied to four specimens in each group by a high-resolution CT scanner (Inveon, Siemens, Germany). After scanning, the data was collected by 3D reconstruction software (Volume Graphics MAX, Volume Graphics, Germany). The 3D images for a region of interest (ROI, Ø 5.5 × 7.0 mm) containing the repair area was reconstructed for further quantitative analysis. Briefly, the osteogenesis indices, including BV/TV (bone volume versus the total volume of defect) and Tb·N (Trabecular Numbers) were quantitatively analyzed from the reconstruction data in the ROIs.

2.7.4. Histological and histomorphometric analysis

Finished with the radiological examination, the specimens ($n = 4$) of each group were fixed in 4% paraformaldehyde solution preparing for histological analysis. After immersion for one week, these specimens were dehydrated by graded alcohol (80%–100%) and followed by embedding in polymethylmethacrylate (PMMA). The embedded specimens were sectioned to a slice with 80–100 μm in thickness form the mid–portion of the repair region by a saw microtome (SP1600, Leica; Germany). Afterwards, the sections were grinded and polished to ~20 μm in thickness by a grinding system (Exakt-Micro, Leica; Germany). Finally, the ultrathin sections were stained by McNeal staining and recorded by a light-resolution microscope (DMLA, Leica; Germany) with different magnifications (× 40, × 200).

As for the histomorphometric analysis, the pictures of sections at the magnifications of 100 were chosen and analyzed by the imaging analytical software Image Pro Plus 6.0 (Media Cybernetic, USA). Both of area of the newly formed bone (BS) and total area (TS) were quantitatively measured, and then the BS/TS was calculated form the collected data ($n = 4$).

2.8. SEM/EDS characterization

The PMMA-embedded, unstained femoral bone sections were coated with carbon, and the compositional and morphological changes of the bioceramic scaffolds *in vivo* were characterized by field-emission scanning electron microscopy (FE-SEM; Hitachi, Tokyo, Japan) and energy-dispersive X-ray spectrometer (EDS; Apollo X; EDAX, Inc., Mahwah, USA) at an accelerating voltage of 15 kV. The Ca/P atomic ratio was determined and four randomly selected regions were chosen for analysis.

2.9. Statistical analysis

The data were analyzed by the statistical software (SPSS 19.0, IBM, USA) and expressed as mean ± SD. Multiple comparisons were measured by One-way ANOVA tests; in addition, the difference between two groups was tested by Student's *t* tests. For all of the statistical results, p value < 0.05 stands for statistically significant.

3. Results

3.1. Primary characterization of bioceramic scaffolds

Fig. 1(A, B) shows the schematic key steps in fabricating bioceramic scaffolds and the different unit cell models. The representative external and internal porous architectures of sintered scaffolds could be visualized by 2D/3D μCT reconstruction, as shown in Fig. 1C. The cubic pore morphology with different pore heights was well retained for the scaffolds even if they had undergone highly thermal sintering. Meanwhile, noticeable increase in pore size and full pore interconnectivity were confirmed from the H200 to H600 scaffolds, which was consistent with the model design. It means the tunable side-wall pore height can be precisely manufactured by digital light processing (DLP)-based stereolithography. The quantitative analysis (Fig. 1D) confirmed that the pore-strut density (BV/TV, Tb·Th) decreased gradually with increasing the pore size, and conversely the BS/BV-representing specific surface area was increased. However, the Tb·N value showed no significantly difference among the four groups of scaffolds. Additionally, a similar linear shrinkage in pore size and uneven decrease of porosity could be found from the sintered scaffolds (Table 1). The phase analysis (Data Not shown) also confirmed the β-wollastonite (PDF #27–0088) for the bioceramic powder for AM process.

3.2. Structural, mechanical and bio-dissolution properties of bioceramic scaffolds

Surface structures of the bioceramic scaffolds with different side-wall pore height were observed by SEM. As shown in Fig. 2A, the top-view surface pores were maintained cubic morphology and similar pore size. The high-magnification SEM micrographs showed that, the surface structures of bioceramic struts were similar to each other, and especially the dense microstructure could be seen on the surface of pore struts. This is attributed to the constant chemical composition of the scaffolds, and dilute Mg substitution may substantially enhance the sintering property of wollastonite bioceramics. Moreover, the pore strut surface could induce apatite-like mineral layer after soaking in SBF for 3 days. The face-scanning EDX spectra showed high enough P peak and the Ca/P was in the range of 1.38–1.52. The side-wall pores exhibited rectangular morphology, but sintering treatment did lead to a significant decrease of pore height. Generally, the pore regularity and interconnectivity could be confirmed by SEM observation (Fig. 2B). The pore height of H200 scaffolds was only ~130 μm, in comparison with that of H600 scaffolds

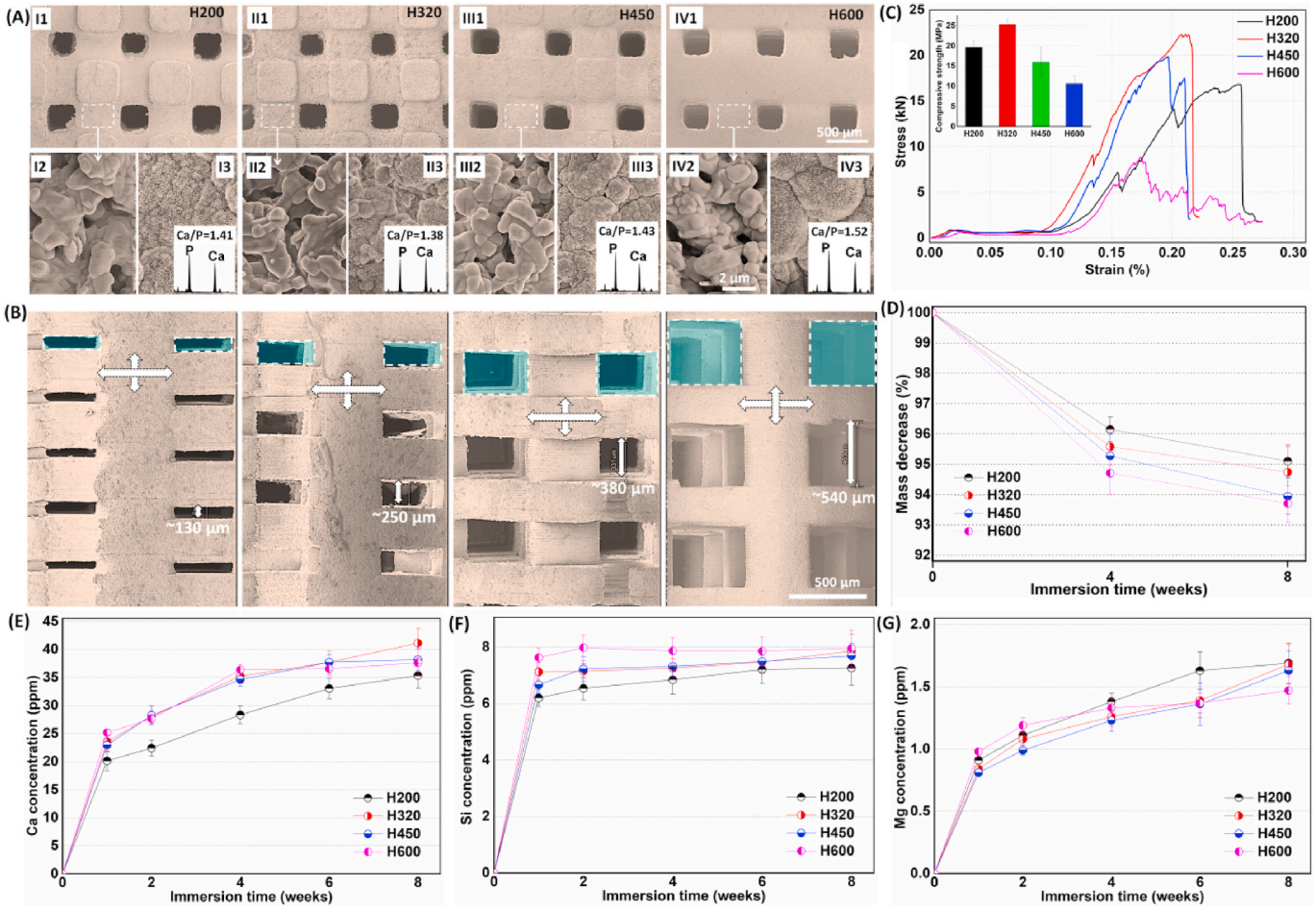

Fig. 2. Primary structural, mechanical and biodissolution characterization of the sintered bioceramic scaffolds with increased side-wall pore height. (A) SEM images of the top-view surface morphology (I1, II1, III1, IV1) and comparison with the surface mcirostructures before (I2, II2, III3, IV2) and after (I3, II3, III3, IV3; insets showing the face-scannning EDX spectra) soaking in SBF; (B) SEM images of the side-wall morphology of the scaffolds (The green frames showing the side-wall macropores; The crossing double-arrows displaying the pore struts with width × height of ~490 × 290 μm; The white arrow showing the height of side-wall macropores); (C) Stress-strain curves of the scaffolds and peak strength (inset); (D) Mass decrease of the scaffolds with different during immersion in Tris buffer for a long time stage; (E–G) Changes in ion concentrations in Tris buffer during immersion process.

(~540 μm).

In order to evaluate the structural stability of the scaffolds *in vivo*, the compressive measurement was carried out on the sintered scaffolds. In context to change in pore sizes during model design, as discussed earlier, although the small pores may contribute to the reduction in porosity (Table 1), the stress-strain curves showed similar response under compression load (Fig. 2C). The H320 scaffolds exhibit appreciable compressive resistance, indicating ~2.5-fold high apparent strength in comparison with the H600 scaffolds (Fig. 2C, inset).

To probe the mass loss in the early stage, a bio-dissolution test was investigated in Tris buffer at physiochemical temperature (37 °C) for the bioceramic scaffolds. As expected, the scaffolds with higher side-wall pore size showed a slightly higher mass loss (4.9%–6.3%; Fig. 2D) within the early 8 weeks. This is probably attributed to the higher.

Specific surface area and faster ion exchange from the larger pores in Tris buffer, which is mildly effective on accelerating bio-dissolution of the scaffolds. In fact, the H600 scaffolds showed higher ion concentrations in the aqueous buffers in the early stage (2 weeks; Fig. 2E–G). However, it is interesting that only the Si concentration was maintained a very stable level (~7–8 ppm) for the four groups of scaffolds after 2 weeks, even if the Ca and Mg ion concentrations exhibited a slight increase with time. It may be interpreted that the silicate groups may reach a saturation point in the buffer medium.

3.3. *In vivo* bone regeneration evaluation for the bioceramic scaffolds

3.3.1. *Macroscopic assessment in vivo*

The different pore size formulations in scaffolds were designed to systematically understand their effects on bone regeneration efficiency *in vivo*. The rabbit models involving the implantation of scaffolds in femoral bone defects were illustrated in Fig. 3A. No rabbits showed infection symptoms, and all of animals were survived long enough until the different time point for specimen harvesting. Gross examination of femur specimens showed that the defects were healing over time and no necrosis was observed in any femoral bone specimen. A mild inflammatory reaction mainly occurred only within the initial two weeks (Fig. 3B). Callus formation partially covered some parts of the implants surface after 4 weeks and the whole surface of the implants was completely covered by the well-organized calluses after 10 weeks.

The radiological examination revealed the scaffolds exhibited different biodegradation progress at 2–16 weeks postoperatively (Fig. 3C). It was observed that the best repair happened in the defects treated with H450 and H600, and the worst belonged to bone defects filled with H200 in the early stage of both four and six weeks. The H200 scaffolds were easily distinguished with the host bone tissue after 10 weeks. This is because the H200 implants had lowest porosity and only underwent a slower biodegradation. In contrast, the H600 bioceramic scaffolds displayed very fast biodegradation *in vivo* during 4–16 weeks

Fig. 3. Animal model operation process and primary evaluation of the femoral bone specimens. (A) The animal operation procedure including femur defect preparation and bioceramic scaffold implantation; (B) Primary μCT reconstruction evaluation post-operatively; (C) Bone specimens at 2 weeks post-operatively; (D, E) X-ray images of the femoral specimens filled with scaffolds after implantation for 2–16 weeks. Rectangular or circular dotted-line frames in (C, D) showing the bone defect positions.

postoperatively. Also, the differences of material residual between the two groups filled with H320 and H450 scaffolds was scarcely determined by X-ray radiography after 16 weeks. It suggests that the macropore size in the side wall orientation may contribute to the new bone tissue ingrowth and biodegradation of CSi-Mg6 pore struts.

3.3.2. *μCT examination in vivo*

Fig. 4(A, B) showed the 2D/3D μCT images of the femoral bone defects at 2 and 4 weeks postoperatively. From the longitudinal and transverse sections, all of implants displayed structurally integral scaffolds and the pore wall was visible in all samples as blue colored struts at the early time stage. The 2D μCT examination revealed that the new bone tissue began to infiltrate the peripheral pores in the H600 scaffolds at 2 weeks, and especially neo-bone.

Distribution in printed channel pores varied from the periphery to the center zone, as a function of the pore size and distance to the native bone/scaffold interface. The H200 and H320 groups showed very limited neo-bone tissue after 4 weeks, even though some bone tissue could grow into the second channel pores of H450 and H600 scaffolds.

With the prolongation of repair time up to 6 weeks, appreciable new bone tissue could invade the macropore constructs in the H450 and H600 groups (Fig. 4C), and even resulted in completely bridging the bone defect after 10 weeks (Fig. 4D). In the case of the H200 and H320 groups, some neo-bone tissue began to fill in the scaffolds after 6 weeks, and the later produced more osteogenesis at this time point. It is well agreed that the interconnected macropore network is the prime requisite for new bone tissue ingrowth through osteogenic cell migration and vascularization. Therefore, the bioceramic scaffolds with increased side-wall pore size presented a significantly enhanced osteogenic efficiency during the early to middle stage repair process.

The spatial distribution of bone tissue in the macropore constructs parallel to longitudinal axis of the scaffolds was evaluated by μCT examination in correspondence with the three main side-wall zones (Ø 5.5, 3.5, 1.5 mm) at the later stage (i.e. 16 weeks; Fig. 5). In terms of different zones over the Volume of Interest (VOI) in the scaffolds, bone formation appeared less uniform in the different zones for the H200 group, having no or hardly observed in the center zone (Ø 1.5 mm; Fig. 5A). However, as for the defect filled with the H320 scaffold, new bone tissue extended to the center region of the implant, throughout the entire porous scaffold (Fig. 5B). Notably, the H450 and H600 groups showed lower matured bone tissue in the center macropores in comparison with the H320 group (Fig. 5C and D).

On the other hand, the quantitative BV/TV and Tb·N values were consistent with the abovementioned observing results (Fig. 6), which responded respectively with the amount of new bone tissue and bone trabecular density in bone defects. Much higher BV/TV data for the H450 and H600 groups at 2–10 weeks implied a sustaining bone tissue ingrowth, resulting in high-efficient bone repair in terms of increased Tb·N data (Fig. 6B). It was interesting that, however, the BV/TV data showed a significant decreasing trend from 10 weeks to 16 weeks in the H600 group. In contrast, an extremely slow increase in TV/TV and Tb·N data for the H200 group indicated the significant difficulty in new bone tissue formation through the small side-wall pores of scaffolds. As for the H320 group, a steady increase in BV/TV and Tb·N values were measured during 6–16 weeks, and even superior to the H450 and H600 group at 16 weeks. It suggests the newly formed bone tissue in these two groups would be preferentially.

Matured and bone remodeled, leading to a transient decrease of quantitated bone tissue in the defect. Moreover, the percentage of remaining bioceramic residuals was significantly lower in the H600 groups than in the H200 group after 16 weeks (Data Not shown), implying a faster biodegradation of the scaffolds with higher pore size.

3.3.3. *Histological evaluation in vivo*

The histological staining analysis aimed to examine whether the scaffolds with large pores had superiority when comparing with the scaffolds with small pores. Once the PMMA-embedded bone specimens were cut transversely, the cross-sectional sections of the scaffold around the circular bone defect were easily observed under light microscope. The McNeal staining images revealed a clearer porous networks and tissue/scaffold interface at 4 weeks. The extent of new bone ingrowth in scaffolds varied within different side-wall pore size (Fig. 7). The H200

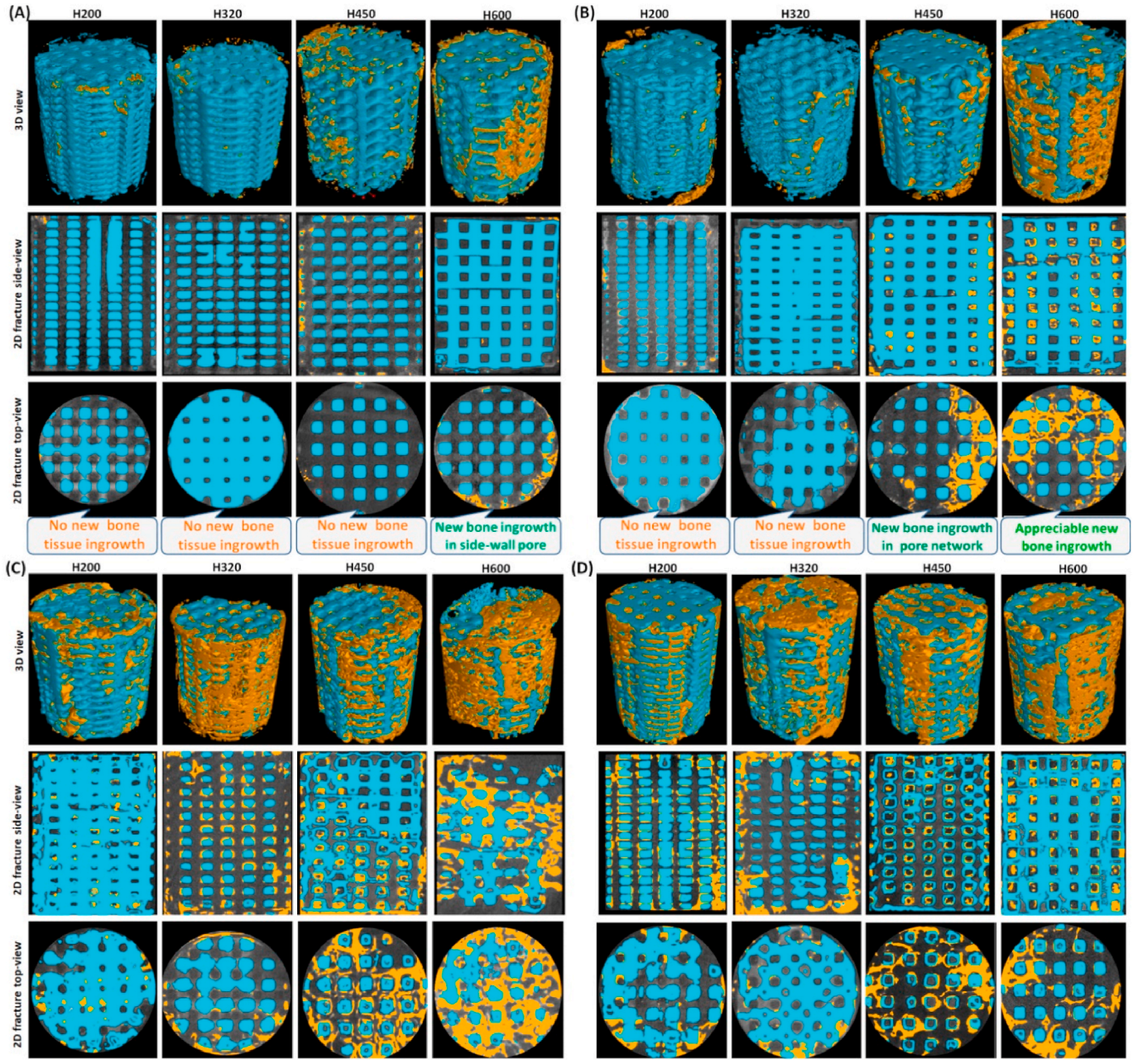

Fig. 4. Representative μCT-reconstructed 3D porous scaffold architectures (top panel; Ø 5.5 × 7.0 mm) and 2D graphs of longitudinal and transverse sections at the early time stage of 2 weeks (A), 4 weeks (B), 6 weeks (C) and 10 weeks (D), respectively. Blue: biomatrial; Yellow: neo-bone tissue.

scaffold could not supply a porous substrate for new bone tissue ingrowth and the non-calcified tissue was predominantly located in scaffold at 4 weeks (Fig. 7A). As for the H320 scaffold, the osteoblasts were undoubtedly favorable for migrating into the peripheral pores, but it was only observed very limited amount of osteoid-like tissue formation at the early stage (Fig. 7B). However, histological analysis (Fig. 7C and D) together with the μCT sections (Fig. 4B) revealed the sustaining connection between the native bone and porous biomaterials, and notably the new bone tissue penetrated into the H450 and H600 scaffolds from the periphery of scaffolds, displaying an expected attachment and integration between the neo-bone tissue and the bioceramic struts.

After 6–16 weeks, the McNeal straining confirmed the mineralization and new bone growth, and the evolution of histology in the tissue-material interface, respectively (Fig. 8A). It was observed that the H450 group maintained a steady osteogenesis response from the periphery to the center zone of scaffold, and finally at 16 weeks, obtained appreciable matured bone tissue in the whole scaffold architectures approximate to that of the H600 group. However, the bone formation was retarded in the H200 and H320 groups, possibly due to the limitation of the small interconnected pores in scaffolds, and especially the former had less newly mineralized tissue after 10 weeks. On the other hand, the bone defect margins could not be easily identified because of appreciable biodegradation of ceramic struts and complete osseous union of the operated site in the H450 and H600 group.

Also, the quantitative morphometric analysis of BS/TS (%) confirmed that the H450 and H600 groups showed appreciable osteogenesis capacity in comparison with the H200 and H320 groups at the early stage, while the new bone formation was degenerated in the later at 16 weeks (Fig. 9). The H450 group showed the highest BS/TS value during the whole implantation process. Meanwhile, the H320 group exhibited a steady increase in bone regeneration capacity but inferior to the H600 group in the later stage.

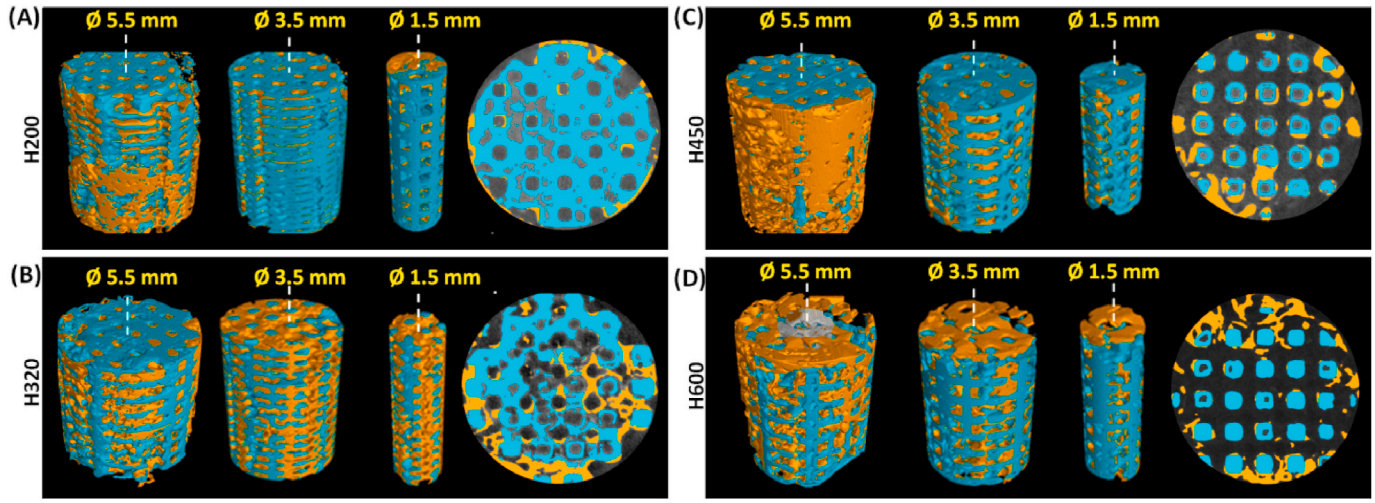

Fig. 5. μCT-reconstructed images of different scaffold zones (Ø 5.5, 3.5, 1.5 × 7.0 mm) parallel to the longitudinal axis over the Volume of Interest (VOI) and 2D transverse section (Ø 5.5 mm) in the H200 (A), H320 (B), H450 (C), and H600 (D) scaffolds at the later time stage of 16 weeks. Blue: biomatrial; Yellow: neo-bone tissue.

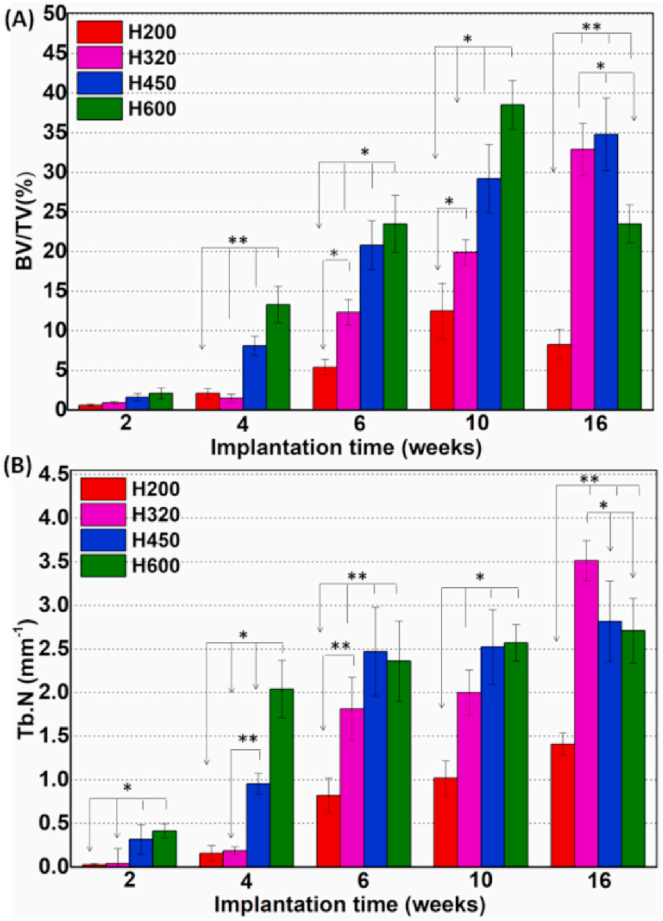

Fig. 6. Quantitative analyses of BV/TV (A), and Tb·N (B) in the bone defects according to the 3D μCT reconstruction analyses after implantation for 2–16 weeks, respectively. $^{*}p < 0.05$; $^{**}p < 0.01$.

3.3.4. *Phase conversion chemical composition evaluation in vivo*

The SEM/EDS analysis was employed to detect the transformation process of Ca-silicate strut to the apatite-like bone mineral and elemental distributions after 6 and 16 weeks, respectively (Fig. 10). In order to distinguish the bioceramic conversion, the ion distributions were arbitrarily divided by different colors in SEM images and EDS mappings. Evidently, unconverted bioceramic struts in bone defect were rich of Si, and the transition layer (new bone tissue zone) was a *P*-rich layer with high Ca concentration. With prolonging time up to 16 weeks, the Mg distribution became more homogenous, accompanying with a gradual decrease of Si-rich zone. The outer layer adjacent to Si-rich zone became thicker, which was presumably the converted apatite mineral layer rich of Ca and P. In particular, the struts in H450 and H600 scaffold almost disappeared with homogeneous Ca or P distribution. Moreover, the Ca/P ratio in the mentioned regions of the scaffolds was listed in the P mapping. The Ca/P ratio in the scaffolds with increase side-wall pore sizes gradually decreased from 2.10 ± 0.10 to 1.24 ± 0.12 at 6 weeks. Simultaneously, the Ca/P ratio in the new bone and the apatite-like layer were increased with prolonging implantation period. The Ca/P ratio (1.40 ± 0.18–1.24 ± 0.22) in the converted (apatite-like) layer at 16 weeks was more below to stoichiometric HA (1.67).

4. Discussion

A variety of pore-making techniques have been offered some promise in designing porous scaffolds. Many investigations have highlighted how the pore interconnection, shape, or size is essential in driving the nutrient transport, vascular infiltration and material biodegradation [4,9,11,16]. Unfortunately, the conventional soft-/hard-template replica methods have met multiple contradictory design criteria that are often difficult to reconcile one or the other to some extent [15,16,36]. In recent years, AM technology has been extensively evaluated to facilitate in fabricating various strut- or curve surface-based scaffolds with precise pore size and complete interconnectivity [25,37,38]. This drives us to clarify the influences of pore structural parameters (i.e. pore size and interconnectivity) on long-term osteo-regeneration performance, avoiding the contradictory results due to poor pore interconnection.

DLP-based stereolithography can readily fabricate porous ceramics with complex geometries, affording good dimensional precision with low cost [30]. This technique is acknowledged to precisely tailor the strut dimension and interconnected pores and even to produce ultra-thin or ultrahigh-porosity materials [26,39,40]. In the present study, the common features are the constant width and height of bioceramic struts (550 × 350 μm) along longitudinal axis in CAD models, so that the porosity of macroporous bioceramics is increased with the increase of side-wall pore height (Table 1). Once the porosity is maintained invariably, however, the strut dimension should be reduced when the

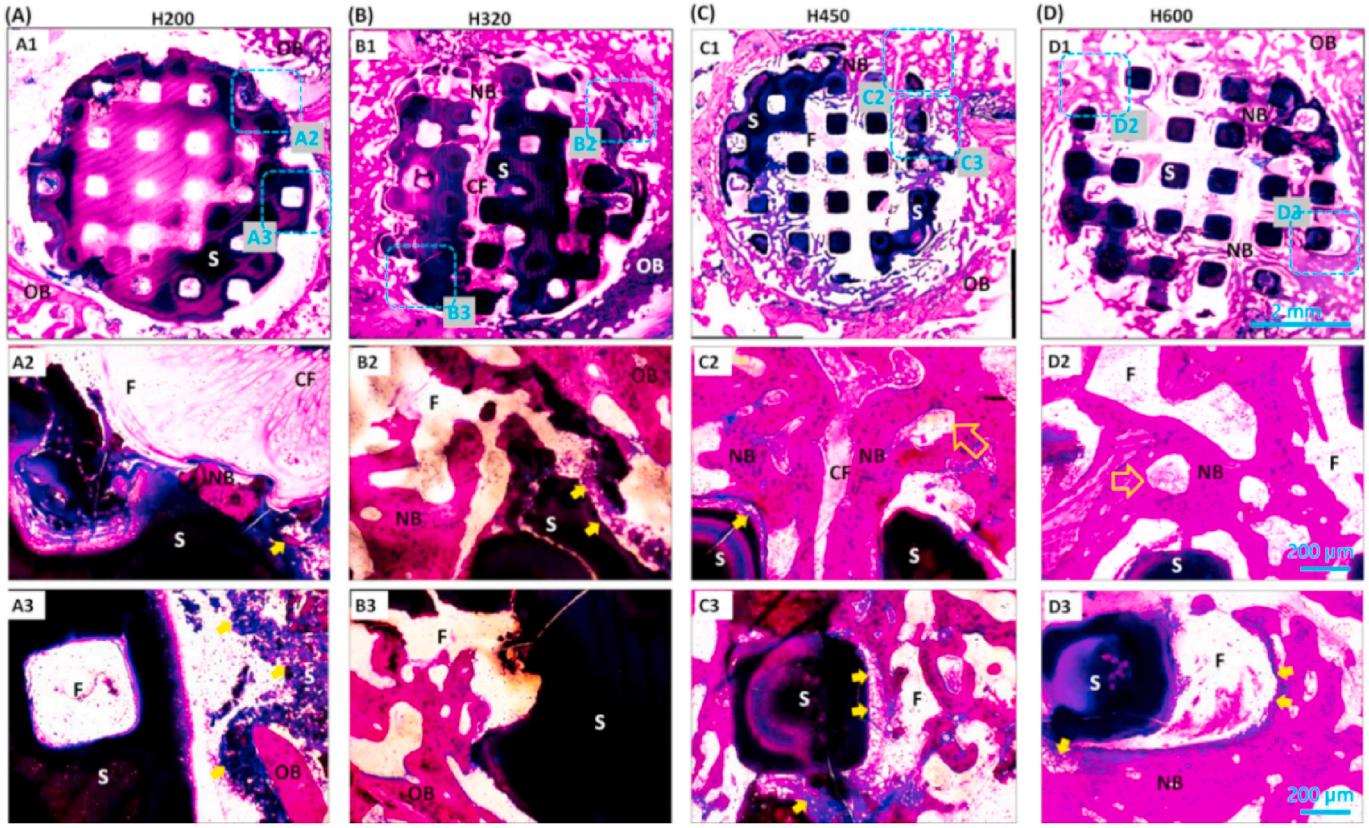

Fig. 7. McNeal-strained light mirographs (40 × , 200 ×) of transverse sections of bone specimens filled with the porous scaffolds of H200 (A), H320 (B), H450 (C), and H600 (D) at 4 weeks of post-implantation. OB: Original maturing bone; NB: Newly formed neo-bone; F: Fibrous tissue; CF: Collagenous, non-calcified fibrous tissue; S: Bioceramic strut; Hollow arrow: newly formed vessels; Solid arrow: interface between native bone and materials.

pore size is increased. This compromising scaffold design is inevitably disadvantageous for studying the relationship between bone formation and pore structural parameters. In comparison with the pore size, the scaffold porosity is less critical for accelerating or delaying the early-time osteoregenerative efficiency *in vivo* [16].

The SEM observation demonstrates that the difference among the CSi-Mg6 scaffolds is mainly the height of side-wall pores (Fig. 2), and especially the precisely controlled pore architecture may be replicated by stereolithography. Our study also showed that the bone tissue ingrowth is directly related to the pore size over the entire time stage, and especially the larger side-wall pores are extremely beneficial for neo-bone tissue invasion in the early stage. μCT has become a popular non-destructive tool for obtaining 3D structural images of scaffolds and regenerated bone tissue [41,42]. In this study, the μCT reconstruction confirmed the completeness of sintered scaffolds and osteoid-like tissue began to infiltrate the peripheral pores within 2 weeks in the H600 scaffolds (Figs. 1 and 4), and after 4 weeks the osteoid tissue abundance in the large-pore scaffolds suggests the neo-bone formation, which is a preliminary step for the maturation toward the lamellar bone. In contrast, the neo-bone ingrowth was still limited in the H320 and H200 scaffolds after 4 and 6 weeks, respectively (Fig. 4). These μCT visualizations, as evidenced by the histological observation, are demonstrated that the early-time bone regeneration is directly dependent on pore dimension.

It is known that, even though the native bone mineral structures exhibit a gradient from cancellous bone to less porous cortical bone, a pore size of over 200 μm has yet been recommended for benefiting new bone tissue ingrowth within porous scaffolds [11,14,43]. The conventional scaffold fabrication techniques could only prepare those with controllable specific pore features including geometry, size, and directionality in comparison with AM technology. Descamps described a microsphere template method to prepare bioceramic scaffolds with high pore interconnectivity [19]. He proposed an organic skeleton shrinkage mechanism to adjust pore interconnection to some extent (from 0.2 to 0.6 times of macropore size). The dimension of each interconnected pore is unable to be precisely tailored, so that it is inevitably difficult to optimize pore construct for osteoregenerative requirement *in vivo* [44,45]. Zhang et al. have reviewed the inverse opal template-derived scaffolds with uniform pore size interconnected network for biomedical applications [46]. Although the macropore size and pore interconnectivity could be easily tuned by changing the diameter of the template granules, the large-scale fabrication of the closely packed microsphere-array template is a challenge because this process is time consuming. Ice-segregation-induced self-assembly is another intriguing strategy to prepare porous biomaterials with highly sophisticated structures. The success in the control of anisotropic pore architecture has attracted much attention to prepare the strength-strong scaffolds [47,48]. However, the very small pore size (usually less than 250 μm) lead to poor cellular and vascular infiltration through the unidirectional pores [49].

Stereolithography technique indicate the flexibility in fabricate the macropore constructs with uniform interconnected pore size in scaffolds (Figs. 1 and 2). All scaffolds showed a fully interconnected pore architecture, and importantly, the dimension of side-wall pores in sintered scaffolds were always maintained like the CAD model, which is of benefit to identify the regenerative progress as a function of pore size with time. In this regard, our investigations indicate the amount of early-stage new bone and non-mineralized tissue is different in the large- and small-pore scaffolds, because the former displays much appreciable bone tissue at the later stage. Nevertheless, the collagenous fibrous tissue preferentially infiltrates through the small-pore scaffolds in the early stage, which would provoke slow osteogenic response and retard the

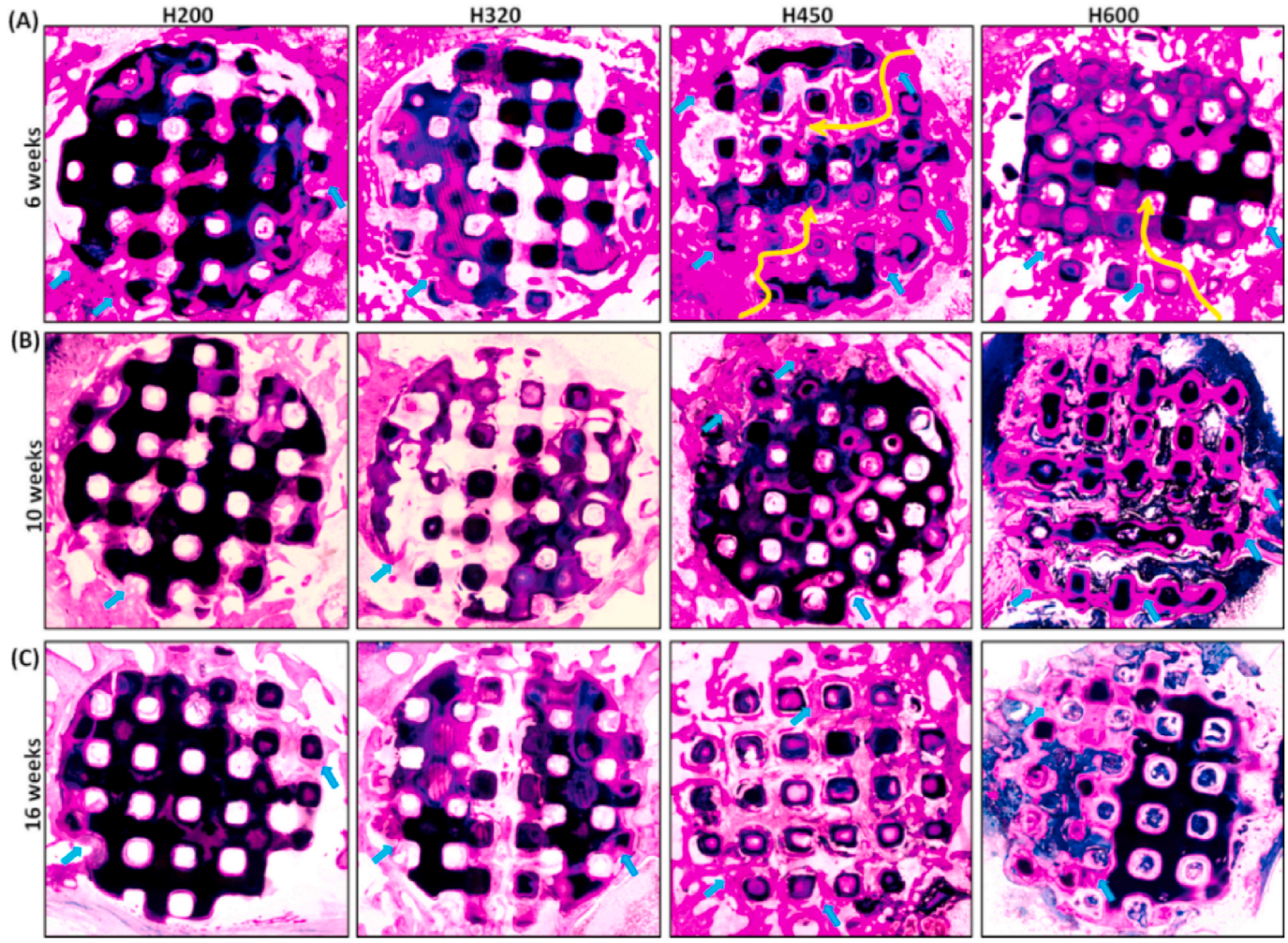

Fig. 8. McNeal-strained light mirographs (40 ×) of transverse sections of bone specimens filled with porous scaffolds at 6 weeks (A), 10 weeks (B), and 16 weeks (C) of post-implantation, respectively. Yellow arrow indicating the bone tissue ingrowth from the periphery to the center zone of the scaffolds. Blue arrow: new bone tissue.

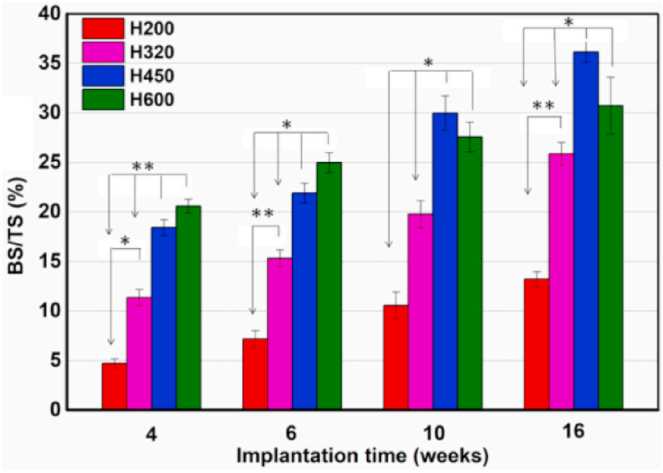

Fig. 9. The percentage of new bone area at different time stages of implantation in each group by using histomophometric analysis. *$p < 0.05$; **$p < 0.01$.

bone healing process *in vivo*. This consistent difference in osteogenic rate, albeit manufactured by the same CSi-Mg bioceramic, as well as its associated with a different bone ingrowth, implies a pore size-dependent osteogenic behavior.

It has long been believed that surface biocompatibility and pore structures constitute to the osteoconduction of biomaterials. Osteostimulation, on the other hand, is attributed to the controlled ion release of bioceramics, and precisely controlling primary pore geometry and spatiotemporal evolution of porous architectures is the source of enhancement of bone regeneration and thereby leads to an improved bone repair [50–53]. Ca-silicate-based biomaterials have great potential for applications in the damaged hard tissue regeneration areas because of their good biocompatibility, excellent osteostimulating properties, and comprehensive foreign ion substitution characteristics [54,55]. They have long been identified as next generation biomaterials and are investigated extensively [56].

Our previous studies have confirmed that the 3%–10% Mg-substituting-Ca could maintain the CSi phase after sintering at ≤1200 °C [33]. Meanwhile, the *in vitro* osteogenic cell activity investigation revealed the excellent surface cytocompatibility and osteogenic activity of the CSi-Mg*x* bioceramics with different Mg substitution ratios from 3% to 10% [57]. Therefore, such nonstoichiometric CSi confirmed in this study, have convincingly shown its osteostimulative activities. Our work shows an active, dissolution-driven biodegradation in Tris buffer and the mass loss of bioceramic scaffolds exhibit a slight dependence on the pore size in pH-buffer aqueous solution *in vitro* (Fig. 2D–G). It is agreed that bio-dissolution can be considered as a factor of biodegradation, and dissolution- and cell-mediated factors may synergistically affect the stability of porous bioceramics. Phosphate

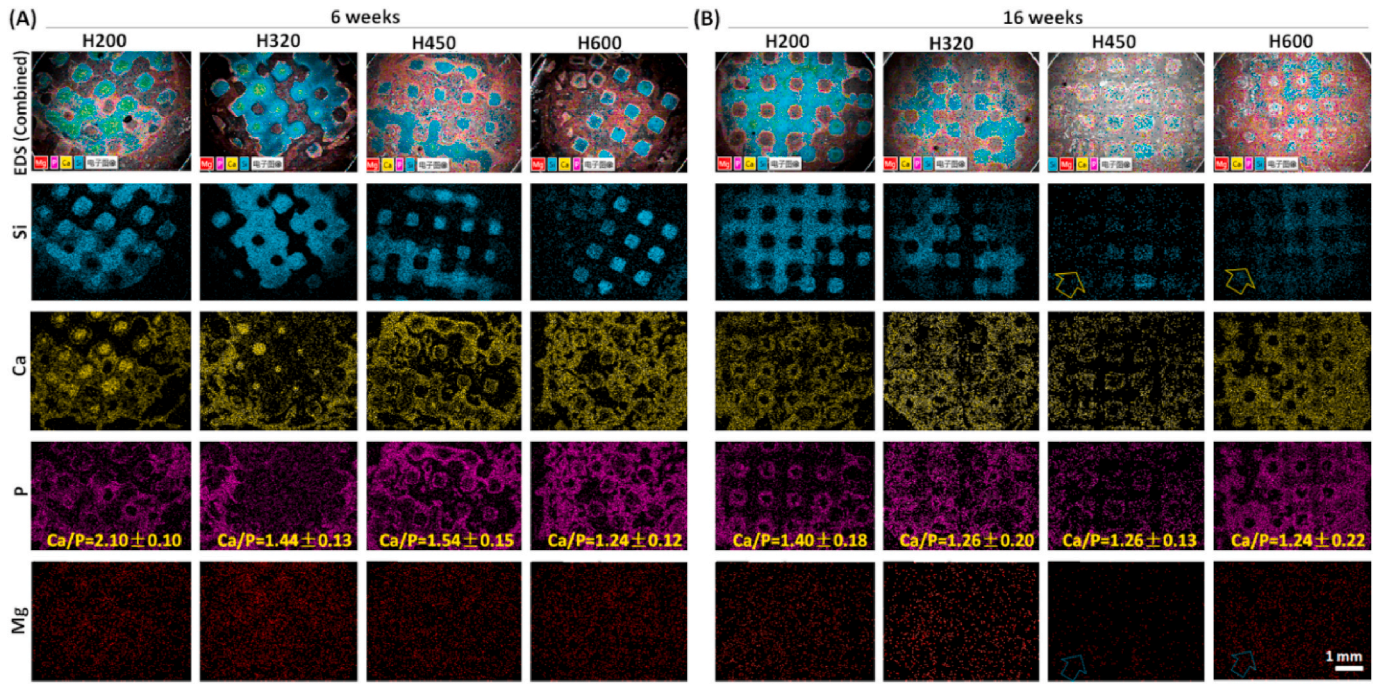

Fig. 10. SEM images and EDS mappings of Si, P, Ca, and Mg for the scaffolds after implantation for 6 weeks (A) and 16 weeks (B) (50 ×). According to the EDS mapping, different components were overlapped on the SEM images to maintain clarity. The mineralized tissue (*P*-rich) formed around the pore strut (Si-rich) of the bioceramic scaffolds.

buffered solution (PBS) is a representative inorganic salt aqueous solution but its pH buffer potential is junior to Tris buffer. Meanwhile, the phosphate group ($H_2PO_4^-$, HPO_4^{2-}) in PBS may induce apatite mineralization on the surface of the silicate bioceramics, so that the solution-mediated biodegradation in PBS may produce mass fluctuation [58].

In the present study, the pore wall and released ions did not appear to provoke any detrimental inflammatory response *in vivo* in the early stage (Figs. 4 and 7). As new bone tissue progressed efficiently in the interconnected macropores and integrated tightly with the bioceramic struts (Fig. 4), the *in vivo* studies at multiple time points (6–16 weeks) also provided clear evidence for intrinsic osteostimulative response in the repair process. In particular, the superior performances of the large-pore H450 and H600 scaffolds as compared to the H200 and H320 counterparts may be attributed to the appreciable pore dimension and ion dissolution products-derived osteostimulative efficacy. Moreover, the H450 scaffolds show more appreciable new bone tissue after 16 weeks in comparison with the H600 groups. The possible reason can be attributed that the faster biodegradation rate in H600 scaffolds leads to larger pore dimension and low-density substrate with time, and thus is suboptimal for osteogenic cell migration and growth.

Histological analysis confirmed the nearly complete bone ingrowth of the defects with new osseous tissue of similar density to the surrounding pre-existing bone in the H450 group (Fig. 8). The larger pores in H600 scaffolds readily enhance the degradation and ion exchange from the pore struts, implying the ion dissolution products would synergistically activate a sustained bone tissue ingrowth. Therefore, more matured bone tissue (i.e. BV/TV data) is formed in the H600 groups after 6 and 10 weeks compared with the other groups (Fig. 6A). It is worthy to note that, although the new bone mineralization in H320 group was inferior to the H450 and H600 groups at 6 and 10 weeks, it produces the highest Tb·N value of ossifying tissue at 16 weeks. μCT analysis also indicated a total of ~33% of the ROI was infused with bone tissue in this group at 16 weeks, implying appreciable biodegradation and bioactive stimulation derived from the ions release. In contrast, limited new bone formation was revealed in the H200 group as <15% of its volume was filled with bone tissue at 10 and 16 weeks. The H200 scaffold has a lower porosity and bioactive ion concentration accumulation (Table 1 & Fig. 2), even though its pores are completely interconnected, with minimum size, curvature, and geometry compatible with that as necessary to permit neo-bone tissue invasion [9,14,46,59].

It is known that the native bones have a remarkable self-healing potential, especially in the small damages as new bone tissue may infiltrate the neighboring defects. However, as for the large bone defect filled with small-pore scaffolds, the areas penetrating to the internal zone of macroporous bioceramics from the host bone have more difficulties in receiving ostogenic cells and nutrients necessary to accelerate new bone growth. In the present experimental results, the bone repair process promoted by the Ca-silicate scaffolds is challenged by reducing the pore dimension in the side-wall orientation, to retard infiltration of osteogenic cells from the host tissue. Conversely, the biodegradation of bioceramic struts in the small-pore scaffolds is slower over time, resulting in detrimental fibrous tissue in growth in the early time stage. While these H200 scaffolds are all valuable to evaluate osteoconduction potential of the biomaterial, this leads to an effective reduction of pore height available to assess the consistency of pore structural parameters, although it did compromise the overall analysis due to much shrinkage of pore structure after sintering treatment. Accordingly, the rationale behind choosing porous biomaterial design is that a simple adjustment of pore structure (pore size and interconnection) in the contact interface between material and native bone could simultaneously tailor the biodegradation and bioactive ion release, and thus confirming that these biomaterials can stimulate efficient bone regeneration and repair within a narrow time window stage.

5. Conclusion

In summary, we developed the bioactive ceramic scaffolds with precisely tuned pore structures by ceramic stereolithography, and systematically evaluated the pore structural parameters and biodegradation behavior *in vitro* and bone regeneration efficacy *in vivo*. Dilute Mg substitution in wollastonite can contribute to a significant enhancement

of mechanical properties beneficial for structural stability; meanwhile, the most elaborative differences in osteogenic efficiency among the four types of scaffolds appear in the early and later stage due to remarkably difference in pore height and osteoconductive properties. The present experimental results, for the first time, provide evidence that precisely tuned pore structure in biocermamic scaffolds with slightly different biodegradation rate exhibit extremely intriguing biological properties in enhancing bone repair. Therefore, it is believed that this versatile CAD model optimization process in manipulating biomaterial (micro)structure offers a convenient route to produce bioactive scaffolds with a rational design toward promising clinical translation.

CRediT authorship contribution statement

Ronghuan Wu: Methodology. **Yifan Li:** Investigation, Writing - original draft. **Miaoda Shen:** Validation. **Xianyan Yang:** Visualization. **Lei Zhang:** Formal analysis. **Xiurong Ke:** Formal analysis. **Guojing Yang:** Supervision. **Changyou Gao:** Data curation. **Zhongru Gou:** Conceptualization, Project administration, Writing - review & editing. **Sanzhong Xu:** Conceptualization, Project administration, Writing - review & editing.

Declaration of competing interest

The authors declare that they have no conflict of interests.

Acknowledgments

Authors would like to acknowledge financial support from the National Key Research and Development Program of China (2017YFE0117700, 2018YC1105401), National Natural Science Foundation of China (81772311, 81871775), and the Science and Technology Department of Zhejiang Province Foundation (LGF18E020001, LGF20H060016).

References

[1] J. Henkel, M.A. Woodruff, D.R. Epari, R. Steck, V. Glatt, I.C. Dickinson, P. F. Choong, M.A. Schuetz, D.W. Hutmacher, Bone regeneration based on tissue engineering conceptions - a 21st century perspective, Bone Res 1 (3) (2013) 216–248.
[2] Y.Y. Filippov, E.D. Orlov, E.S. Klimashina, P.V. Evdokimov, T.V. Safronova, V. I. Putlayev, J.V. Rau, Colloidal forming of macroporous calcium pyrophosphate bioceramics in 3D-printed molds, Bioact Mater 5 (2) (2020) 309–317.
[3] E. Babaie, S.B. Bhaduri, Fabrication aspects of porous biomaterials in Orthopedic applications: a review, Acs Biomaterials Science & Engineering 4 (1) (2018) 1–39.
[4] R.A. Perez, S.J. Seo, J.E. Won, E.J. Lee, J.H. Jang, J.C. Knowles, H.W. Kim, Therapeutically relevant aspects in bone repair and regeneration, Mater. Today 18 (10) (2015) 573–589.
[5] W. Wang, K.W.K. Yeung, Bone grafts and biomaterials substitutes for bone defect repair: a review, Bioact Mater 2 (4) (2017) 224–247.
[6] R. De Santis, A. Gloria, T. Russo, U. D'Amora, S. Zeppetelli, A. Tampieri, T. Herrmannsdörfer, L. Ambrosio, A route toward the development of 3D magnetic scaffolds with tailored mechanical and morphological properties for hard tissue regeneration: preliminary study, Virtual Phys. Prototyp. 6 (4) (2011) 189–195.
[7] H. Petite, V. Viateau, W. Bensaid, A. Meunier, C. de Pollak, M. Bourguignon, K. Oudina, L. Sedel, G. Guillemin, Tissue-engineered bone regeneration, Nat. Biotechnol. 18 (9) (2000) 959–963.
[8] Y. Huang, C. Wu, X. Zhang, J. Chang, K. Dai, Regulation of immune response by bioactive ions released from silicate bioceramics for bone regeneration, Acta Biomater. 66 (2018) 81–92.
[9] A.A. Zadpoor, Bone tissue regeneration: the role of scaffold geometry, Biomater Sci 3 (2) (2015) 231–245.
[10] A. Hoppe, A.R. Boccaccini, Biological impact of bioactive Glasses and their dissolution products, Front Oral Biol 17 (2015) 22–32.
[11] V. Karageorgiou, D. Kaplan, Porosity of 3D biomaterial scaffolds and osteogenesis, Biomaterials 26 (27) (2005) 5474–5491.
[12] S. Derakhshanfar, R. Mbeleck, K. Xu, X. Zhang, W. Zhong, M. Xing, 3D bioprinting for biomedical devices and tissue engineering: a review of recent trends and advances, Bioact Mater 3 (2) (2018) 144–156.
[13] T. Russo, U. D'Amora, A. Gloria, M. Tunesi, M. Sandri, S. Rodilossi, D. Albani, G. Forloni, C. Giordano, A. Cigada, A. Tampieri, R. De Santis, L. Ambrosio, Systematic analysis of injectable materials and 3D Rapid prototyped magnetic scaffolds: from CNS applications to soft and hard tissue repair/regeneration, Procedia Engineering 59 (2013) 233–239.
[14] S.W. Choi, Y. Zhang, M.R. Macewan, Y. Xia, Neovascularization in biodegradable inverse opal scaffolds with uniform and precisely controlled pore sizes, Adv Healthc Mater 2 (1) (2013) 145–154.
[15] A.C. Jones, C.H. Arns, D.W. Hutmacher, B.K. Milthorpe, A.P. Sheppard, M. A. Knackstedt, The correlation of pore morphology, interconnectivity and physical properties of 3D ceramic scaffolds with bone ingrowth, Biomaterials 30 (7) (2009) 1440–1451.
[16] P. Kasten, I. Beyen, P. Niemeyer, R. Luginbuhl, M. Bohner, W. Richter, Porosity and pore size of beta-tricalcium phosphate scaffold can influence protein production and osteogenic differentiation of human mesenchymal stem cells: an in vitro and in vivo study, Acta Biomater. 4 (6) (2008) 1904–1915.
[17] R. Dhandapani, P.D. Krishnan, A. Zennifer, V. Kannan, A. Manigandan, M.R. Arul, D. Jaiswal, A. Subramanian, S.G. Kumbar, S. Sethuraman, Additive manufacturing of biodegradable porous orthopaedic screw, Bioact Mater 5 (3) (2020) 458–467.
[18] D.L. Wheeler, K.E. Stokes, R.G. Hoellrich, D.L. Chamberland, S.W. McLoughlin, Effect of bioactive glass particle size on osseous regeneration of cancellous defects, J. Biomed. Mater. Res. 41 (4) (1998) 527–533.
[19] M. Descamps, T. Duhoo, F. Monchau, J. Lu, P. Hardouin, J.C. Hornez, A. Leriche, Manufacture of macroporous beta-tricalcium phosphate bioceramics, J. Eur. Ceram. Soc. 28 (1) (2008) 149–157.
[20] G.F.D. Labate, G. Catapano, C. Vitale-Brovarone, F. Baino, Quantifying the micro-architectural similarity of bioceramic scaffolds to bone, Ceram. Int. 43 (12) (2017) 9443–9450.
[21] J. Rolecek, L. Pejchalova, F.J. Martinez-Vazquez, P.M. Gonzalez, D. Salmon, Bioceramic scaffolds fabrication: indirect 3D printing combined with ice-templating vs. robocasting, J. Eur. Ceram. Soc. 39 (4) (2019) 1595–1602.
[22] F.J. O'Brien, Biomaterials & scaffolds for tissue engineering, Mater. Today 14 (3) (2011) 88–95.
[23] Z. Chen, Z. Li, J. Li, C. Liu, C. Lao, Y. Fu, C. Liu, Y. Li, P. Wang, Y. He, 3D printing of ceramics: a review, J. Eur. Ceram. Soc. 39 (4) (2019) 661–687.
[24] C. Wang, W. Huang, Y. Zhou, L. He, Z. He, Z. Chen, X. He, S. Tian, J. Liao, B. Lu, Y. Wei, M. Wang, 3D printing of bone tissue engineering scaffolds, Bioact Mater 5 (1) (2020) 82–91.
[25] P. Diloksumpan, R.V. Bolanos, S. Cokelaere, B. Pouran, J. de Grauw, M. van Rijen, R. van Weeren, R. Levato, J. Malda, Orthotopic bone regeneration within 3D printed bioceramic scaffolds with region-dependent porosity gradients in an equine model, Adv Healthc Mater 9 (10) (2020), e1901807.
[26] S.M. Bittner, J.L. Guo, A. Melchiorri, A.G. Mikos, Three-dimensional printing of multilayered tissue engineering scaffolds, Mater. Today 21 (8) (2018) 861–874.
[27] M.O. Wang, C.E. Vorwald, M.L. Dreher, E.J. Mott, M.H. Cheng, A. Cinar, H. Mehdizadeh, S. Somo, D. Dean, E.M. Brey, J.P. Fisher, Evaluating 3D-printed biomaterials as scaffolds for vascularized bone tissue engineering, Adv. Mater. 27 (1) (2015) 138–144.
[28] M. Zhang, R. Lin, X. Wang, J. Xue, C. Deng, C. Feng, H. Zhuang, J. Ma, C. Qin, L. Wan, J. Chang, C. Wu, 3D printing of Haversian bone-mimicking scaffolds for multicellular delivery in bone regeneration, Sci Adv 6 (12) (2020) eaaz6725.
[29] M. Layani, X. Wang, S. Magdassi, Novel materials for 3D printing by photopolymerization, Adv. Mater. 30 (41) (2018), e1706344.
[30] H. Quan, T. Zhang, H. Xu, S. Luo, J. Nie, X. Zhu, Photo-curing 3D printing technique and its challenges, Bioact Mater 5 (1) (2020) 110–115.
[31] J.J. Xie, H.F. Shao, D.S. He, X.Y. Yang, C.L. Yao, J. Ye, Y. He, J.Z. Fu, Z.R. Gou, Ultrahigh strength of three-dimensional printed diluted magnesium doping wollastonite porous scaffolds, Mrs Communications 5 (4) (2015) 631–639.
[32] A. Liu, M. Sun, H. Shao, X. Yang, C. Ma, D. He, Q. Gao, Y. Liu, S. Yan, S. Xu, Y. He, J. Fu, Z. Gou, The outstanding mechanical response and bone regeneration capacity of robocast dilute magnesium-doped wollastonite scaffolds in critical size bone defects, J. Mater. Chem. B 4 (22) (2016) 3945–3958.
[33] J. Xie, X. Yang, H. Shao, J. Ye, Y. He, J. Fu, C. Gao, Z. Gou, Simultaneous mechanical property and biodegradation improvement of wollastonite bioceramic through magnesium dilute doping, J Mech Behav Biomed Mater 54 (2016) 60–71.
[34] X.Y. Li, K.H. Hu, Z.G. Lu, Effect of light attenuation on polymerization of ceramic suspensions for stereolithography, J. Eur. Ceram. Soc. 39 (7) (2019) 2503–2509.
[35] F. Lu, R. Wu, M. Shen, L. Xie, M. Liu, Y. Li, S. Xu, L. Wan, X. Yang, C. Gao, Z. Gou, Rational design of bioceramic scaffolds with tuning pore geometry by stereolithography: microstructure evaluation and mechanical evolution, J. Eur. Ceram. Soc. (2020), https://doi.org/10.1016/j.jeurceramsoc.2020.10.002.
[36] M.C. von Doernberg, B. von Rechenberg, M. Bohner, S. Grunenfelder, G.H. van Lenthe, R. Muller, B. Gasser, R. Mathys, G. Baroud, J. Auer, In vivo behavior of calcium phosphate scaffolds with four different pore sizes, Biomaterials 27 (30) (2006) 5186–5198.
[37] O. Al-Ketan, R. Rowshan, R.K. Abu Al-Rub, Topology-mechanical property relationship of 3D printed strut, skeletal, and sheet based periodic metallic cellular materials, Additive Manufacturing 19 (2018) 167–183.
[38] S. Gomez, M.D. Vlad, J. Lopez, E. Fernandez, Design and properties of 3D scaffolds for bone tissue engineering, Acta Biomater. 42 (2016) 341–350.
[39] O. Guillaume, M.A. Geven, V. Varjas, P. Varga, D. Gehweiler, V.A. Stadelmann, T. Smidt, S. Zeiter, C. Sprecher, R.R.M. Bos, D.W. Grijpma, M. Alini, H. Yuan, G. R. Richards, T. Tang, L. Qin, L. Yuxiao, P. Jiang, D. Eglin, Orbital floor repair using patient specific osteoinductive implant made by stereolithography, Biomaterials 233 (2020) 119721.
[40] A.A. Zadpoor, Meta-biomaterials, Biomater Sci 8 (1) (2019) 18–38.
[41] A.C. Daly, P. Pitacco, J. Nulty, G.M. Cunniffe, D.J. Kelly, 3D printed microchannel networks to direct vascularisation during endochondral bone repair, Biomaterials 162 (2018) 34–46.

[42] J.R. Jones, G. Poologasundarampillai, R.C. Atwood, D. Bernard, P.D. Lee, Non-destructive quantitative 3D analysis for the optimisation of tissue scaffolds, Biomaterials 28 (7) (2007) 1404–1413.
[43] S.W. Choi, J. Xie, Y. Xia, Chitosan-based inverse opals: three-dimensional scaffolds with uniform pore structures for cell culture, Adv. Mater. 21 (29) (2009) 2997–3001.
[44] Z. Wang, Z. Guo, H. Bai, J. Li, X. Li, G. Chen, J. Lu, Clinical evaluation of beta-TCP in the treatment of lacunar bone defects: a prospective, randomized controlled study, Mater Sci Eng C Mater Biol Appl 33 (4) (2013) 1894–1899.
[45] F. Bai, Z. Wang, J. Lu, J. Liu, G. Chen, R. Lv, J. Wang, K. Lin, J. Zhang, X. Huang, The correlation between the internal structure and vascularization of controllable porous bioceramic materials in vivo: a quantitative study, Tissue Eng. 16 (12) (2010) 3791–3803.
[46] Y.S. Zhang, C. Zhu, Y. Xia, Inverse opal scaffolds and their biomedical applications, Adv. Mater. 29 (33) (2017).
[47] Q. Cheng, C. Huang, A.P. Tomsia, Freeze casting for assembling bioinspired structural materials, Adv. Mater. 29 (45) (2017).
[48] S. Flauder, U. Gbureck, F.A. Muller, Structure and mechanical properties of beta-TCP scaffolds prepared by ice-templating with preset ice front velocities, Acta Biomater. 10 (12) (2014) 5148–5155.
[49] X.Y. Peng, M. Hu, F. Liao, F. Yang, Q.F. Ke, Y.P. Guo, Z.H. Zhu, La-Doped mesoporous calcium silicate/chitosan scaffolds for bone tissue engineering, Biomater Sci 7 (4) (2019) 1565–1573.
[50] L.H. Lei, Y.M. Wei, Z.X. Wang, J.Y. Han, J.W. Sun, Y. Chen, X.Y. Yang, Y.M. Wu, L. L. Chen, Z.R. Gou, Core-shell bioactive ceramic robocasting: tuning component distribution beneficial for highly efficient alveolar bone regeneration and repair, Acs Biomaterials Science & Engineering 6 (4) (2020) 2376–2387.
[51] J. Fu, C. Zhuang, J. Qiu, X. Ke, X. Yang, Z. Jin, L. Zhang, G. Yang, L. Xie, S. Xu, C. Gao, Z. Gou, Core-shell biphasic microspheres with tunable density of shell micropores providing tailorable bone regeneration, Tissue Eng. 25 (7–8) (2019) 588–602.
[52] H. Autefage, F. Allen, H.M. Tang, C. Kallepitis, E. Gentleman, N. Reznikov, K. Nitiputri, A. Nommeots-Nomm, M.D. O'Donnell, C. Lange, B.M. Seidt, T.B. Kim, A.K. Solanki, F. Tallia, G. Young, P.D. Lee, B.F. Pierce, W. Wagermaier, P. Fratzl, A. Goodship, J.R. Jones, G. Blunn, M.M. Stevens, Multiscale analyses reveal native-like lamellar bone repair and near perfect bone-contact with porous strontium-loaded bioactive glass, Biomaterials 209 (2019) 152–162.
[53] X. Chen, X. Sun, X. Yang, L. Zhang, M. Lin, G. Yang, C. Gao, Y. Feng, J. Yu, Z. Gou, Biomimetic preparation of trace element-codoped calcium phosphate for promoting osteoporotic bone defect repair, J. Mater. Chem. B 1 (9) (2013) 1316–1325.
[54] F. Deng, W. Zhai, Y. Yin, C. Peng, C. Ning, Advanced protein adsorption properties of a novel silicate-based bioceramic: a proteomic analysis, Bioact Mater 6 (1) (2021) 208–218.
[55] P. Zhou, D. Xia, Z. Ni, T. Ou, Y. Wang, H. Zhang, L. Mao, K. Lin, S. Xu, J. Liu, Calcium silicate bioactive ceramics induce osteogenesis through oncostatin M, Bioact Mater 6 (3) (2021) 810–822.
[56] L.L. Hench, J.M. Polak, Third-generation biomedical materials, Science 295 (5557) (2002) 1014–1017.
[57] M. Sun, A. Liu, H. Shao, X. Yang, C. Ma, S. Yan, Y. Liu, Y. He, Z. Gou, Systematical evaluation of mechanically strong 3D printed diluted magnesium doping wollastonite scaffolds on osteogenic capacity in rabbit calvarial defects, Sci. Rep. 6 (2016).
[58] J. Wang, L. Zhang, X. Sun, X. Chen, K. Xie, M. Lin, G. Yang, S. Xu, W. Xia, Z. Gou, Preparation and in vitro evaluation of strontium-doped calcium silicate/gypsum bioactive bone cement, Biomed. Mater. 9 (4) (2014), 045002.
[59] S.J.P. Callens, R.J.C. Uyttendaele, L.E. Fratila-Apachitei, A.A. Zadpoor, Substrate curvature as a cue to guide spatiotemporal cell and tissue organization, Biomaterials 232 (2020) 119739.